

## Multifrequency EPR Investigation of Dimanganese Catalase and Related Mn(III)Mn(IV) Complexes

K.-O. Schäfer,<sup>†</sup> R. Bittl,<sup>\*,‡</sup> F. Lendzian,<sup>†</sup> V. Barynin,<sup>§</sup> T. Weyhermüller,<sup>||</sup> K. Wieghardt,<sup>||</sup> and W. Lubitz<sup>\*,||</sup>

Max-Volmer-Laboratorium für Biophysikalische Chemie, Technische Universität Berlin, D-10623 Berlin, Germany, Fachbereich Physik, Freie Universität Berlin, D-14195 Berlin, Germany, Department of Molecular Biology and Biotechnology, University of Sheffield, Sheffield S10 2TN, United Kingdom, and Max-Planck-Institut für Strahlenchemie, D-45470 Mülheim, Germany

Received: April 19, 2002; In Final Form: September 11, 2002

The superoxidized Mn<sup>III</sup>Mn<sup>IV</sup> state of dimanganese catalase from *Thermus thermophilus* and a series of structurally similar Mn<sup>III</sup>Mn<sup>IV</sup> complexes were investigated using continuous wave (CW) and pulsed EPR spectroscopy at X- (9 GHz), Q- (34 GHz), and W-band (94 GHz) frequencies. The bis( $\mu$ -oxo) or bis( $\mu$ -oxo)-( $\mu$ -carboxylato) bridged complexes exhibit strong antiferromagnetic coupling ( $|J| > 100 \text{ cm}^{-1}$ ). Relevant EPR parameters ( $G$ - and <sup>55</sup>Mn hyperfine coupling tensors) are obtained by spectral simulations and yield a consistent data set for all frequency bands. Two mechanisms that lead to EPR line broadening are discussed. The advantage of our fitting strategy, i.e., precise determination of the  $G$ -tensor from high-field/frequency and hyperfine couplings from low-frequency EPR spectra, over conventional procedures is outlined. Comparison of the  $G$ - and <sup>55</sup>Mn hyperfine tensors of the model complexes with those of dimanganese catalase show that both values are sensitive probes for small structural changes.

### Introduction

Catalases are redox-enzymes that catalyze the disproportionation of H<sub>2</sub>O<sub>2</sub> into O<sub>2</sub> and H<sub>2</sub>O. While most catalases contain iron in the active site, there are also dimanganese catalases, which are found in *Thermus thermophilus*, *Thermoleophilum album*, and *Lactobacillus plantarum*.<sup>1–4</sup> Recently, detailed structural information for dimanganese catalase from *L. Plantarum*<sup>5</sup> and *Th. thermophilus*<sup>6</sup> was obtained by an ultrahigh-resolution X-ray diffraction analysis on single crystals. The catalase from the latter consists of six identical subunits with a combined mass of 200 kDa. Two manganese ions are incorporated into each subunit. The oxidation states of the ions could be determined by EPR and EXAFS spectroscopy. It was shown that in the catalytic cycle, the states Mn<sup>II</sup>Mn<sup>II</sup> and Mn<sup>III</sup>Mn<sup>III</sup> are involved.<sup>7–9</sup> Additionally, an intermediate Mn<sup>II</sup>Mn<sup>III</sup> state and a superoxidized Mn<sup>III</sup>Mn<sup>IV</sup> state exist. Along with the change in oxidation states, the bridging ligands between the two manganese ions are assumed to change during the catalytic cycle. Since the exchange coupling is mediated via these bridges, any variation in the electronic structure of the bridge will have a large influence on the exchange coupling constant  $J$ . From X-ray diffraction, it was shown that the Mn ions are linked by  $\mu$ -oxo bridges. However,  $\mu$ -oxo,  $\mu$ -hydroxo, or  $\mu$ -aquo could not be distinguished. It was proposed that the Mn<sup>III</sup>Mn<sup>III</sup> state is coupled ferromagnetically via  $\mu$ -hydroxo bridges.<sup>10</sup> For the paramagnetic Mn<sup>II</sup>Mn<sup>III</sup> and Mn<sup>III</sup>Mn<sup>IV</sup> states a protonated bridge should give rise to a large <sup>1</sup>H hyperfine coupling. For the Mn<sup>III</sup>Mn<sup>IV</sup> state, this has so far not been observed in ENDOR

experiments.<sup>11</sup> Further evidence for a  $\mu$ -oxo ligation in the Mn<sup>III</sup>-Mn<sup>IV</sup> state arises from comparison with inorganic models where in most cases this type of bridging ligand is observed. Very recently, different mechanistic models have been investigated on the basis of theoretical calculations.<sup>12,13</sup>

The Mn<sup>II</sup>Mn<sup>III</sup> and Mn<sup>III</sup>Mn<sup>IV</sup> states show a  $S = 1/2$  ground state and are accessible by EPR spectroscopy.<sup>7,14–16</sup> Data of *Th. thermophilus* at 9 GHz have been published by Zheng et al.,<sup>17</sup> and a multifrequency (3, 9, and 16 GHz) analysis for *L. plantarum* has been performed by Haddy et al.<sup>18</sup> Both  $G$ - and <sup>55</sup>Mn hyperfine tensors exhibit large anisotropies. At frequencies below 34 GHz, spectra are dominated by the hyperfine structure, while at higher frequencies, the  $G$ -anisotropy is dominant. The interplay of anisotropies renders an analysis difficult, if only one dominant interaction is taken into account. There might be a considerable uncertainty in the published data, since only low-frequency bands were used. Reliable simulations are only obtained at 94 GHz due to the fact that (i) second and higher order corrections for the hyperfine interaction are less important, and (ii) the resolution of  $G$ -tensor components is increased. Our approach is therefore to precisely determine the  $G$ -tensor at 94 GHz, and then adjust the hyperfine parameters at 9 GHz frequency. This procedure will be tested on model complexes for which 9 and 34 GHz data exist<sup>19</sup> and then applied to the Mn<sup>III</sup>Mn<sup>IV</sup> state of dimanganese catalase.<sup>20–23</sup>

Multifrequency high-field EPR has previously been performed on a series of Mn<sup>III</sup>Mn<sup>IV</sup> complexes.<sup>24</sup> One difficulty so far has been background signals from Mn<sup>II</sup>. These can be introduced by the synthetic procedures or by reduction of the complexes in the presence of, e.g., water or alcohol. Using pulsed EPR-techniques, it is possible to discriminate unwanted Mn<sup>II</sup> impurities and Mn<sup>III</sup>Mn<sup>IV</sup> signals.<sup>25</sup> These unpaired high-field spectra can then be used to obtain EPR parameters with high accuracy.

\* Authors to whom correspondence should be addressed. E-mail: Robert.Bittl@physik.fu-berlin.de; lubitz@mpi-muelheim.mpg.de.

<sup>†</sup> Technische Universität Berlin.

<sup>‡</sup> Freie Universität Berlin.

<sup>§</sup> University of Sheffield.

<sup>||</sup> Max-Planck-Institut.

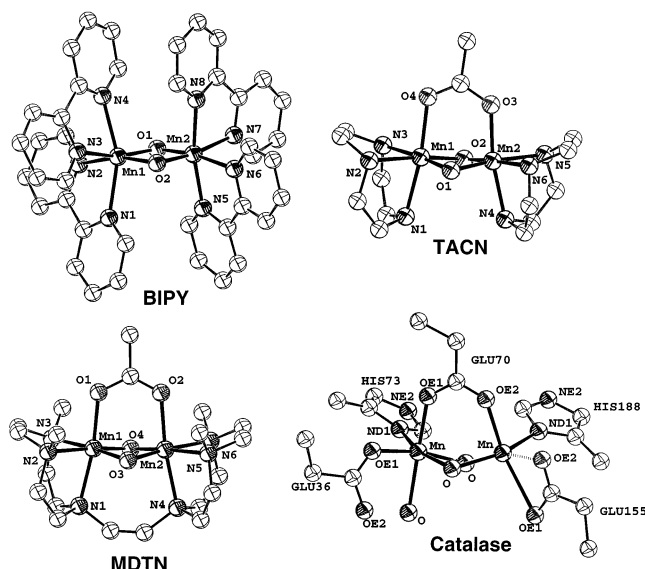


**Figure 1.** Crystal structures of the investigated complexes. Atoms without labels are carbon atoms; hydrogen atoms are not shown. The oxidation state of the Mn ions can be discerned in the structures only for BIPY (Mn1 = Mn<sup>III</sup>, Mn2 = Mn<sup>IV</sup>). Structures of PHEN and DTNE are similar to those of BIPY and MDTN. Top left: BIPY.<sup>48</sup> Top right: TACN.<sup>49</sup> Bottom left: MDTN.<sup>19</sup> Bottom right: dimanganese catalase from *Th. Thermophilus* in the Mn<sup>III</sup>Mn<sup>III</sup> state at 1.0 Å resolution.<sup>6</sup>

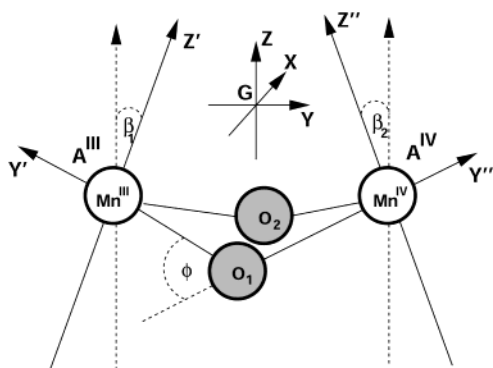


**Figure 2.** Molecular coordinate system for catalase and the dinuclear manganese complexes. The  $\mu$ -oxo  $\mu$ -carboxylato bridged species exhibit a tilt in the Mn<sup>III</sup>–O<sub>1</sub>–O<sub>2</sub>, Mn<sup>IV</sup>–O<sub>1</sub>–O<sub>2</sub> plane. The declination is described by the angle  $\phi$ . The Euler angles  $\beta_1$  and  $\beta_2$  rotate the Mn<sup>III</sup> and Mn<sup>IV</sup> hyperfine tensor axis systems relative to the effective  $G$ -tensor axis system in the indicated way. For simplicity, the effective  $G$ -tensor is assumed to symmetrically correlate with the molecular structure. For BIPY and PHEN,  $\phi = 0$  and the  $y$ -axis is the axis joining the Mn-ions and the  $z$ -axis is the normal vector of the Mn<sup>III</sup>–O<sub>1</sub>–O<sub>2</sub>–Mn<sup>IV</sup> plane.

## Materials and Methods

The dinuclear model complexes BIPY: [Mn<sup>III</sup>Mn<sup>IV</sup>( $\mu$ -O)<sub>2</sub>-bipy<sub>4</sub>]ClO<sub>4</sub>, bipy = bipyridine, PHEN: [Mn<sup>III</sup>Mn<sup>IV</sup>( $\mu$ -O)<sub>2</sub>phen<sub>4</sub>]ClO<sub>4</sub>, phen = *o*-phenanthroline, TACN: [Mn<sup>III</sup>Mn<sup>IV</sup>( $\mu$ -O)<sub>2</sub>( $\mu$ -OAc)tacn<sub>2</sub>]BPh<sub>4</sub>, tacn = 1,4,7-triazacyclononane, DTNE: [Mn<sup>III</sup>Mn<sup>IV</sup>( $\mu$ -O)<sub>2</sub>( $\mu$ -OAc)dtne]BPh<sub>4</sub>, dtne = 1,2-di-(1,4,7-triazacyclononyl)-ethane, and MDTN: [Mn<sup>III</sup>Mn<sup>IV</sup>( $\mu$ -O)<sub>2</sub>( $\mu$ -OAc)-me<sub>4</sub>dtne]BPh<sub>4</sub> were prepared using published procedures.<sup>19</sup> The structures of some complexes obtained from X-ray crystallography are shown in Figure 1. To facilitate the comparison with DFT calculations, we use the same molecular coordinate system as Delfs et al.,<sup>26</sup> which is shown in Figure 2.

The EPR measurements were performed on frozen solutions using dimethylformamide (DMF) for TACN, DTNE, and MDTN or a mixture of CH<sub>2</sub>Cl<sub>2</sub>/CH<sub>3</sub>CN (3:1) for BIPY and PHEN as solvent. Concentrations were typically 1–2 mmol/L.

To avoid traces of water, the solvents (UVASOL spectroscopy grade, Fa. Merck) were dried over 3 Å molecular sieves.

A sample of dimanganese catalase from *Th. thermophilus* was prepared as described previously.<sup>3</sup> The Mn<sup>III</sup>Mn<sup>IV</sup> oxidation state was prepared according to published procedures<sup>15</sup> using an excess of KIO<sub>4</sub> to ensure complete oxidation. The enzyme was suspended in 10 mM phosphate buffer (pH 6.8), the concentration was about 5 mmol/L. Under the experimental conditions used, no signals from other oxidation states were present in the EPR spectra.

The 94 GHz EPR measurements were performed on a Bruker E680 Eleksys spectrometer. The setup for experiments at 9 and 34 GHz has been described previously.<sup>19</sup> To compare CW and pulsed EPR spectra, the field-swept echo spectra were treated with a lab-written pseudomodulation routine.

To obtain  $G$ - and <sup>55</sup>Mn hyperfine tensors, simulations were done using a lab-written computer program that calculates the resonance positions by second-order perturbation theory. It was shown by Haddy et al.<sup>18</sup> that, at 9 GHz, third order corrections to the EPR parameters are smaller than 0.5% and thus a second-order treatment is sufficient for this frequency. For each hf-tensor, three Euler angles are needed to describe the orientation of its principal axis system with respect to the  $G$ -tensor axis system. Determination of these parameters is carried out using a Levenberg–Marquardt fit algorithm that minimizes the mean square deviation ( $\chi^2$ ) between experimental and simulated spectra. Hydrogen and nitrogen hyperfine and higher order manganese quadrupolar splittings are not resolved in the EPR spectra. However, these unresolved splittings contribute to the width of the EPR lines. This was taken into account by a convolution of the spectra using a Gaussian line shape of appropriate width.

The spin Hamiltonian for an exchange coupled dimanganese complex

$$\hat{H} = -2J\vec{S}_1\vec{S}_2 + \beta\vec{B}\vec{g}_1\vec{S}_1 + \beta\vec{B}\vec{g}_2\vec{S}_2 + \vec{S}_1\vec{a}_1\vec{I}_1 + \vec{S}_2\vec{a}_2\vec{I}_2 + \vec{S}_1\vec{d}_1\vec{S}_1 + \vec{S}_2\vec{d}_2\vec{S}_2 \quad (1)$$

includes the isotropic exchange coupling  $J$ , the  $g$ -, zero-field splitting (ZFS), and hyperfine coupling tensors for the two Mn-ions  $\vec{g}_1$ ,  $\vec{g}_2$ ,  $\vec{d}_1$ ,  $\vec{d}_2$ ,  $\vec{a}_1$ , and  $\vec{a}_2$ , respectively. In the complexes, the antiferromagnetic exchange is much larger than the other interactions (strong coupling limit), thus the eigenstates of this Hamiltonian can be grouped according to the total spin  $S = |S_1 - S_2|, \dots, S_1 + S_2$ . At low temperatures, only the  $S = 1/2$  ground state is populated and observed in EPR experiments. Using the spin-coupling model, the spin Hamiltonian in the coupled representation for the ground state is

$$\hat{H} = \beta\vec{B}\vec{G}\vec{S} + \vec{S}\vec{A}_1\vec{I}_1 + \vec{S}\vec{A}_2\vec{I}_2 \quad (2)$$

where  $\vec{S}$  is the total electron spin and  $\vec{G}$  is the  $g$ -tensor of the coupled system,  $\vec{I}_1$  and  $\vec{I}_2$  are the nuclear spins of the Mn<sup>III</sup> and Mn<sup>IV</sup> ions, and  $\vec{A}_1$  and  $\vec{A}_2$  are the effective Mn<sup>III</sup> and Mn<sup>IV</sup> hf coupling tensors. The coupled quantities can be calculated from the uncoupled ones by use of the spin-coupling model.<sup>27,28</sup> Detailed equations for a Mn<sup>III</sup>Mn<sup>IV</sup> system can be found in Zheng et al.<sup>17</sup>

In principle, there could be a magnetic field dependence of the hyperfine couplings  $\vec{A}_i$  and in particular the  $\vec{G}$ -tensor due to magnetic field induced perturbations of the electronic states. However, Krzystek et al.<sup>29</sup> have shown that in Mn<sup>III</sup> monomers a linear field/frequency relation for the resonance condition holds up to a frequency of 550 GHz. This implies constant  $\vec{G}$ -tensor and ZFS up to this microwave frequency. Moreover, the energy

differences between the Mn *d*-orbitals in the Mn<sup>III</sup>Mn<sup>IV</sup> state of catalase and synthetic complexes were measured with UV/vis and MCD spectroscopy<sup>30</sup> and found to be much larger than the Zeeman energy at 3.3 T. Therefore field-independent *G*-tensor and hyperfine couplings can be expected for the systems and the magnetic field range investigated here.

## Results and Discussion

**Evaluation of Spectra.** We started the simulations of the model complexes with the data set published previously<sup>19</sup> using the spin Hamiltonian in eq 2. For the catalase, the data given by Zheng et al.<sup>17</sup> were used. Fitting was restricted to *G*-tensors only for the 94 GHz spectra. The improved *G*-parameters were then applied to simulations at 9 and 34 GHz. If necessary, hyperfine parameters were adjusted in the 9 GHz simulations. The fitting cycle was then restarted with the improved data set. This procedure was terminated when no further improvement of the spectral simulations could be achieved yielding parameters consistent for all three frequency bands.

Due to the complexity of the experimental spectra, a full set of EPR parameters can be obtained only via spectral simulations. Because of the large number of independent variables, a global minimum is not easily found using only one frequency band, e.g., 9 GHz. Fortunately, *G* and hyperfine parameters scale differently for different microwave frequencies, therefore it is possible to determine the parameters more reliably by our multifrequency approach. High-frequency EPR has only been available commercially for a relatively short time. Therefore, multifrequency EPR has been limited to lower frequencies, typically 3, 9, 16, and 34 GHz. However, as we have shown,<sup>19</sup> even at 34 GHz, *G*- and hyperfine anisotropies are of comparable magnitude and therefore not well separated. At lower frequencies, most spectral features are reproduced by finding correct hf-tensors. A variation of the *G*-tensor has little impact on the spectra. Thus the error in the determined *G*-components can be quite large. Moreover, at low frequencies EPR spectra are complicated by higher order hyperfine effects. At high-field, the *G*-tensor can be determined very accurately (e.g., at 94 GHz 0.1 mT corresponds to  $\Delta G = 6 \times 10^{-5}$ ). Because of the large Zeeman energy, the second-order terms are small. With an accurately determined *G*-tensor, the hyperfine tensors can then be adjusted at frequencies where the hyperfine anisotropy is dominant, e.g., at 9 GHz. The reduction of the number of free parameters in the fit then leads to a higher reliability of the hf-tensors. Using this simulation approach, we have confidently determined the EPR parameters for all species. These data are shown in Table 1. The best results were obtained with nonzero Euler angle  $\beta^{50}$  for all inorganic compounds. This angle describes the declination of the *z*-axis (s. Figure 2). For the dimanganese catalase, the assumption that *G*- and hyperfine tensor axes are collinear turned out to be sufficient.

**Spectral Features at Different Frequencies.** The 94 GHz spectra of the model complexes and the dimanganese catalase were recorded at low temperatures (*T* = 20 K) in either CW or pulsed mode. It was possible to obtain CW spectra of highly purified TACN, DTNE, and MDTN that contained no visible Mn<sup>II</sup> impurities. Impurities from Mn<sup>II</sup> ions (*S* = 5/2, *I* = 5/2) give rise to six sharp EPR lines which are particularly pronounced at high frequencies. They arise from the  $m_s = -1/2 \leftrightarrow 1/2$  transition. These lines are seen even when the Mn<sup>II</sup> concentration is very low and so far these impurities have been a major obstacle in high-field EPR on dimanganese systems.<sup>24</sup> Lines from other transitions are broadened by ZFS and are usually not seen in cw mode.

**TABLE 1: Effective *G* and Mn<sup>III</sup> and Mn<sup>IV</sup> hyperfine coupling tensor principal values for the binuclear complexes<sup>a</sup>**

complex		<i>G</i>	<b>A</b> <sup>III</sup> [mT]	<b>A</b> <sup>IV</sup> [mT]	<i>G</i> <sub>iso</sub>	<b>A</b> <sup>III</sup> <sub>iso</sub> [mT]	<b>A</b> <sup>IV</sup> <sub>iso</sub> [mT]
<b>DTNE</b>	<i>x</i>	2.0013	−14.5	7.9	1.9942	−13.9	7.4
	<i>y</i>	1.9974	−16.8	6.9			
	<i>z</i>	1.9838	−10.6	7.6			
<b>MDTN</b>	<i>x</i>	2.0026	−15.0	7.9	1.9939	−14.4	7.5
	<i>y</i>	1.9961	−17.2	6.9			
	<i>z</i>	1.9830	−11.2	7.7			
<b>TACN</b>	<i>x</i>	2.0025	−14.7	7.9	1.9960	−13.8	7.6
	<i>y</i>	2.0005	−16.4	7.1			
	<i>z</i>	1.9851	−10.5	8.0			
<b>BIPY</b>	<i>x</i>	1.9990	−17.9	7.5	1.9913	−16.2	7.8
	<i>y</i>	1.9932	−17.1	7.7			
	<i>z</i>	1.9817	−13.4	8.3			
<b>PHEN</b>	<i>x</i>	1.9992	−17.9	7.6	1.9917	−16.1	7.9
	<i>y</i>	1.9940	−17.1	7.7			
	<i>z</i>	1.9821	−13.3	8.3			
<b>MnCat</b>	<i>x</i>	2.0048	−15.2	8.0	1.9988	−13.5	8.5
	<i>y</i>	2.0040	−14.7	8.3			
	<i>z</i>	1.9876	−10.7	9.1			
<b>MnCat<sup>b</sup></b>	<i>x</i>	2.008	−15.1	8.1	2.002	−13.8	8.4
	<i>y</i>	2.008	−15.1	8.1			
	<i>z</i>	1.990	−11.1	8.9			
<b>MnCat<sup>c</sup></b>	<i>x</i>	2.014	−14.6	8.4	2.009	−13.7	8.5
	<i>y</i>	2.014	−15.2	8.0			
	<i>z</i>	2.000	−11.2	9.0			

<sup>a</sup> The tensor components were obtained from a simultaneous fit of 9, 34, and 94 GHz EPR spectra, see text. Errors:  $\Delta g = \pm 1 \times 10^{-4}$ ,  $\Delta A^{\text{III}} = \pm 0.4$  mT,  $\Delta A^{\text{IV}} = \pm 0.2$  mT. <sup>b</sup> Ref 18. <sup>c</sup> Ref 17.

There are several experimental techniques that can be used to eliminate interfering signals, when chemical sample purification is unsuccessful or the sample is not stable in solution. For example, in continuous wave (CW) mode one could vary the temperature and microwave power. The disadvantage is that the signal of the saturated species usually adds to the background and often suitable experimental conditions cannot be found. It is therefore more convenient to use pulsed EPR techniques which allow for more selective experiments that make use of different *T*<sub>1</sub> and/or *T*<sub>2</sub> relaxation times in different species.<sup>31</sup> Another method to separate the Mn<sup>II</sup> from the Mn<sup>III</sup>Mn<sup>IV</sup> signals is based on different transition moments of species with different electron spin, in this case Mn<sup>II</sup> (*S* = 5/2) and Mn<sup>III</sup>Mn<sup>IV</sup> (*S* = 1/2).<sup>25</sup>

The spectra of BIPY, PHEN, and dimanganese catalase contained various amounts of Mn<sup>II</sup>. By using pulsed techniques these signals were eliminated in BIPY and PHEN by different *T*<sub>2</sub> relaxation times, whereas in the dimanganese catalase the separation was based on different transition moments. Experimental EPR spectra at 9 GHz (X-band), 34 GHz (Q-band), and 94 GHz (W-band) are shown in Figures 3–5 for BIPY, TACN, and the dimanganese catalase, respectively, along with the spectral simulations. The 9 GHz spectrum of BIPY (see Figure 3) consists of more than 16 resolved lines. Additionally, shoulders can be identified at low field, while at high field, the lines appear to be further split. On the high field side, the last line has the shape of a perpendicular tensor component. On the low field side this is not as pronounced, but still visible. This is an indication that the symmetry is nearly axial and the hyperfine anisotropy is larger than the *G*-anisotropy. The 34 GHz spectrum looks quite different from that at 9 GHz. Most pronounced is the shift of first derivative peak intensity from the center of the spectrum (9 GHz) to the high field side (34 GHz). Also, the spectral width—measured from the first peak to the last peak—increased from 125.7 mT to 130.4 mT. Since the hf-anisotropy is frequency independent, this is an indication



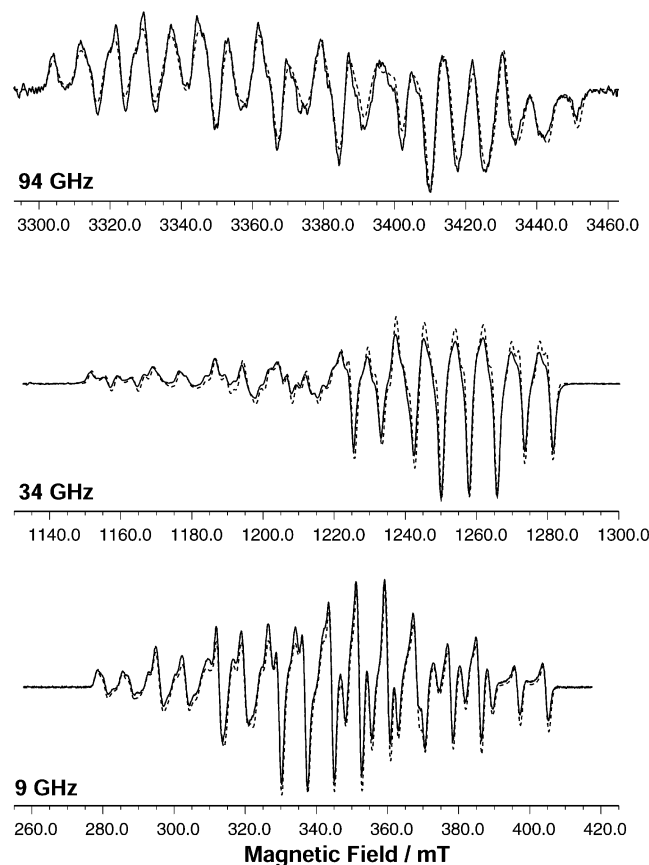


**Figure 3.** Experimental 94, 34, and 9 GHz EPR spectra of model complex BIPY (solid line) and simulations (dotted line) using a consistent data set for the three frequencies (see Table 1).  $\text{Mn}^{II}$  signals in the 94 GHz spectrum were eliminated by  $T_2$  separation. Shown here is the pseudomodulated FSE spectrum. Note that the same field scale (160 mT) has been used for all three spectra. Experimental conditions: X-band:  $\nu_{\text{MW}}$ : 9.60 GHz,  $P_{\text{MW}}$ : 50  $\mu\text{W}$ , mod.amp.(12.5 kHz): 1 G,  $T$ : 10 K, 4 scans in 672 s. Q-band:  $\nu_{\text{MW}}$ : 33.98 GHz,  $P_{\text{MW}}$ : 3  $\mu\text{W}$ , mod.amp.(12.5 kHz): 2 G,  $T$ : 40 K, 1 scan in 168 s. W-band:  $\nu_{\text{MW}}$ : 94.09 GHz, shot rep. 1000  $\mu\text{s}$ ,  $\pi$ -pulse length: 400 ns, interpulse delay  $\tau$ : 1200 ns,  $T$ : 20 K.

of increased  $G$ -anisotropy. When the frequency is further increased to 94 GHz, the shape of the outermost lines is characteristic of components of a rhombic tensor. Clearly, the  $G$ -anisotropy is now much larger than the hf-anisotropy. The spectral width of the 94 GHz spectrum has increased further (to 147.4 mT). We conclude that the hyperfine anisotropy and the unresolved hyperfine broadening dominates the spectrum at frequencies below 34 GHz, while above 34 GHz the  $G$ -anisotropy is dominant. The intensity is distributed rather evenly over the whole spectrum, resembling more closely the case at 9 GHz than at 34 GHz. Finally, the increase in line widths from 9 to 94 GHz suggests a frequency dependent line broadening mechanism.

For the complex TACN (Figure 4), the distribution of line intensities and the shape of the outer lines are comparable to BIPY at 9 GHz. The sharp axial features of the high field side of the BIPY spectrum, however, are broadened, suggesting more rhombic hyperfine tensors. The spectral width is with 115.2 mT small compared to BIPY. At 34 GHz, the high field side of the TACN spectrum is comparable to that of BIPY, while they differ drastically on the low field side. A loss of intensity in the derivative mode on the low field side is not seen for TACN. Furthermore, the first lines still can be attributed to a nearly axial tensor. The spectral width is only increased by 2.8 mT to

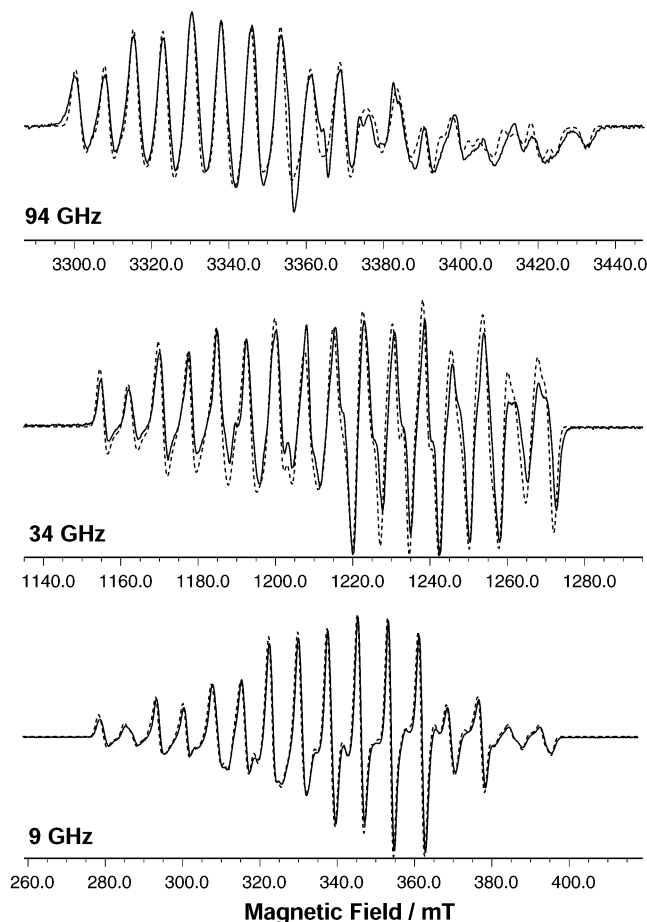


**Figure 4.** Experimental 94, 34, and 9 GHz EPR spectra of model complex TACN (solid lines) and simulations (dotted line) using a consistent data set for the three frequencies (see Table 1). Note that the same field scale (160 mT) has been used for all three spectra. Experimental conditions: X-band:  $\nu_{\text{MW}}$ : 9.46 GHz,  $P_{\text{MW}}$ : 50  $\mu\text{W}$ , mod.amp.(12.5 kHz): 1 G,  $T$ : 20 K, 4 scans in 672 s. Q-band:  $\nu_{\text{MW}}$ : 34.00 GHz,  $P_{\text{MW}}$ : 6  $\mu\text{W}$ , mod.amp.(12.5 kHz): 2 G,  $T$ : 40 K, 1 scan in 168 s. W-band:  $\nu_{\text{MW}}$ : 94.18 GHz,  $P_{\text{MW}}$ : 80 nW, mod.amp.(20.0 kHz): 5 G,  $T$ : 20 K, 1 scan in 672 s.

118.0 mT. These facts suggest that either the hf-anisotropy is larger for TACN than for BIPY or the  $G$ -anisotropy is smaller in TACN than in BIPY. At 94 GHz, a loss in intensity is observed on the high field side. In contrast to BIPY, the shape of the first line does not change significantly from 9 to 94 GHz. The increase of spectral width to 132.2 mT ( $\Delta = 14.2$  mT) is again larger than from 9 to 34 GHz, but slightly smaller compared to BIPY. An increase in line width is noted for TACN (see Figure 4), too.

Finally we want to discuss the spectrum of dimanganese catalase (Figure 5). The most striking difference between catalase and the synthetic complexes is the much smaller line width and therefore the very good spectral resolution at all three frequencies. At 9 GHz, the first two lines on the low and high field side are highly symmetric in shape and are characteristic for axial hyperfine tensor symmetry. As in the previous cases, the hyperfine interaction dominates the  $G$ -anisotropy. The high field part looks quite similar to that of BIPY. Notable are the two sharp features in the center of the spectrum which are not found in the other 9 GHz spectra. The spectral width is within the error margins equal to that of TACN (115.4 mT). Interestingly, the same is true for the 34 GHz spectrum (118.0 mT). Also in agreement with TACN, there is almost no change in the shape of the outer four lines. Thus, the rhombicity ( $G_x - G_y$ )

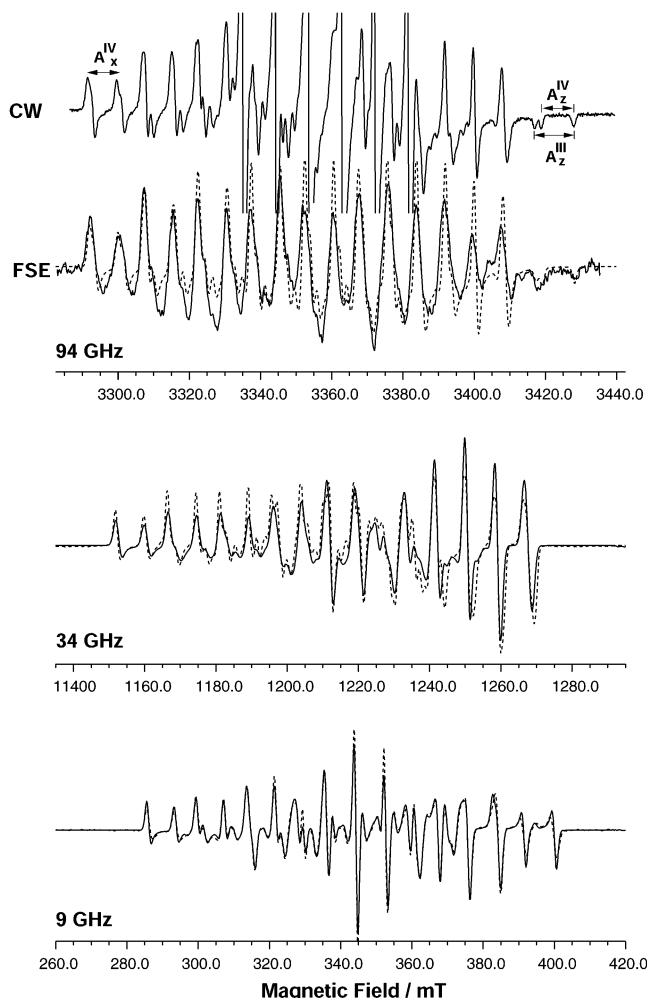


**Figure 5.** Experimental 94, 34, and 9 GHz EPR spectra (solid lines) and simulations (dotted lines) of dimanganese catalase from *Th. thermophilus* in the  $\text{Mn}^{\text{III}}\text{Mn}^{\text{IV}}$  state.  $\text{Mn}^{\text{II}}$  impurities in the 94 GHz FSE spectrum were eliminated using pulsed techniques (see ref 25). The 94 GHz CW spectrum (top) shows a better resolution than the pseudomodulated FSE spectrum, but contains  $\text{Mn}^{\text{II}}$  lines. The identified hyperfine splittings  $A_x^{\text{IV}}$ ,  $A_z^{\text{IV}}$ , and  $A_z^{\text{III}}$  are indicated. Experimental conditions: X-band:  $\nu_{\text{MW}}$  9.66 GHz,  $P_{\text{MW}}$ : 50  $\mu\text{W}$ , mod.amp.(12.5 kHz): 2 G,  $T$ : 30 K, 4 scans in 336 s. Q-band:  $\nu_{\text{MW}}$  33.98 GHz,  $P_{\text{MW}}$ : 50  $\mu\text{W}$ , mod.amp.(12.5 kHz): 2 G,  $T$ : 30 K, 4 scans in 336 s. W-band (CW):  $\nu_{\text{MW}}$  94.08 GHz,  $P_{\text{MW}}$ : 16 nW, mod.amp.(10.0 kHz): 2 G,  $T$ : 20 K, 4 scans in 1376 s.

is very small. The first derivative peak intensities are very similar throughout the whole spectrum. At 94 GHz, the spectral width increases to 136.6 mT ( $\Delta = 18.6$  mT), which exceeds that found for BIPY. Thus, the  $G$ -anisotropy in catalase is larger than in BIPY. Due to the very good resolution of the CW mode spectrum, the three peaks on the high field side can be used to directly extract information about the hf coupling. The splittings are indicated in Figure 5, top. In the spectra of the model complexes these two peaks are not split because of the larger line widths. On the basis of their shape, they are assigned to the same  $G$ -tensor orientation ( $z$ ). The smaller splitting can then be attributed to  $A_z^{\text{IV}}$  and the larger to  $A_z^{\text{III}}$ . Note that both splittings are similar in magnitude. A ratio  $|A_z^{\text{III}}/A_z^{\text{IV}}| = 2$  is predicted by simple spin-coupling theory (neglect of ZFS) assuming that  $a_z^{\text{III}} = a_z^{\text{IV}}$ .<sup>32</sup> In monomeric  $\text{Mn}^{\text{III}}$  complexes,  $A_z^{\text{III}}$  is usually somewhat smaller (e.g.,  $-52.8 \times 10^{-4} \text{ cm}^{-1}$  in  $\text{TiO}_2$ <sup>33</sup>) than in  $\text{Mn}^{\text{IV}}$  (e.g.,  $-72.7 \times 10^{-4} \text{ cm}^{-1}$  in  $\text{TiO}_2$ <sup>34</sup>), therefore a smaller ratio  $|A_z^{\text{III}}/A_z^{\text{IV}}|$  is not unexpected. On the low field side of the spectrum, the separation of the peaks as indicated can be

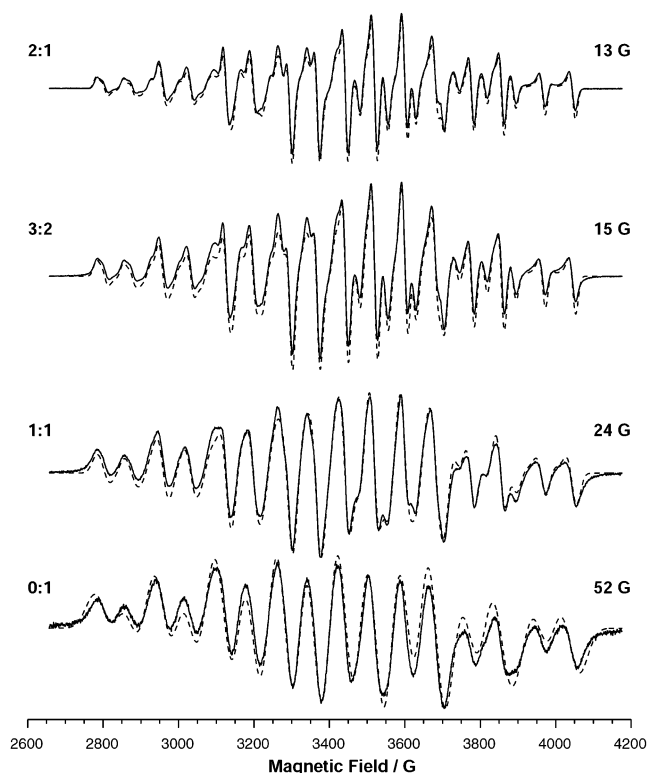


**Figure 6.** 9 GHz EPR spectra of BIPY in  $\text{CH}_3\text{CN}$  with varying amounts of  $\text{CH}_2\text{Cl}_2$ . The concentration of BIPY was kept constant at about 1 mmol/L. Line widths were determined by simulation of the spectra with fixed  $G$ - and hf-tensors. The  $\text{CH}_3\text{CN}/\text{CH}_2\text{Cl}_2$  ratios are shown on the left and the line widths used in the simulation on the right. Experimental conditions:  $\nu_{\text{MW}}$ : 9.4 GHz,  $P_{\text{MW}}$ : 10  $\mu\text{W}$ ,  $T$ : 20 K.

attributed to a hyperfine splitting for the  $G_x$ -tensor component,  $A_x^{\text{IV}}$  (see also Figure 7). Together with the resonance positions which yield information about the  $G$ -tensor, we can extract five of the 12 tensor components, thereby reducing the number of free variables, so that this spectrum can be evaluated accurately, even though  $\text{Mn}^{\text{II}}$  lines impair the middle part of the spectrum. Line widths at 94 GHz (1.1 mT) are only slightly larger than at 9 GHz (1.0 mT).

**Solvent Effects.** Only a few solvents can be used to dissolve the complexes BIPY and PHEN. They have to be strongly polar and redox inert. It is known, for example, that use of ethanol as a solvent leads to formation of monomeric  $\text{Mn}^{\text{II}}$  complexes. One of the solvents used here is  $\text{CH}_3\text{CN}$ . In pure frozen  $\text{CH}_3\text{CN}$ , broad lines were observed at 9 GHz using concentrations where spin-spin interactions can usually be neglected (1 mmol/L). The concentration had to be lowered considerably (to 0.1 mmol/L) to produce better resolved spectra. However, when  $\text{CH}_2\text{Cl}_2$ , in which BIPY is insoluble, is added to the  $\text{CH}_3\text{CN}$  solution, highly resolved spectra were obtained even at concentrations of 1 mmol/L and above. To demonstrate this effect, a series of BIPY spectra with the concentration kept constant at 1 mmol/L and varying  $\text{CH}_2\text{Cl}_2/\text{CH}_3\text{CN}$  ratios is shown in Figure 6. Constant small line widths are found for  $\text{CH}_2\text{Cl}_2/\text{CH}_3\text{CN}$  ratios greater 2:1. Mixtures of  $\text{CH}_2\text{Cl}_2/\text{CH}_3\text{CN}$  are known to form a glassy matrix upon freezing at ratios of about 2:1 to 3:1. Glasses generally yield better resolved spectra due to the more homogeneous microenvironment of the complexes in these matrixes, but at ratios greater than 3:1 no macroscopic glass effect is visible and line widths are still small. The concentration dependence observed in pure  $\text{CH}_3\text{CN}$  suggests that in this solvent BIPY and PHEN have a tendency to form aggregates,

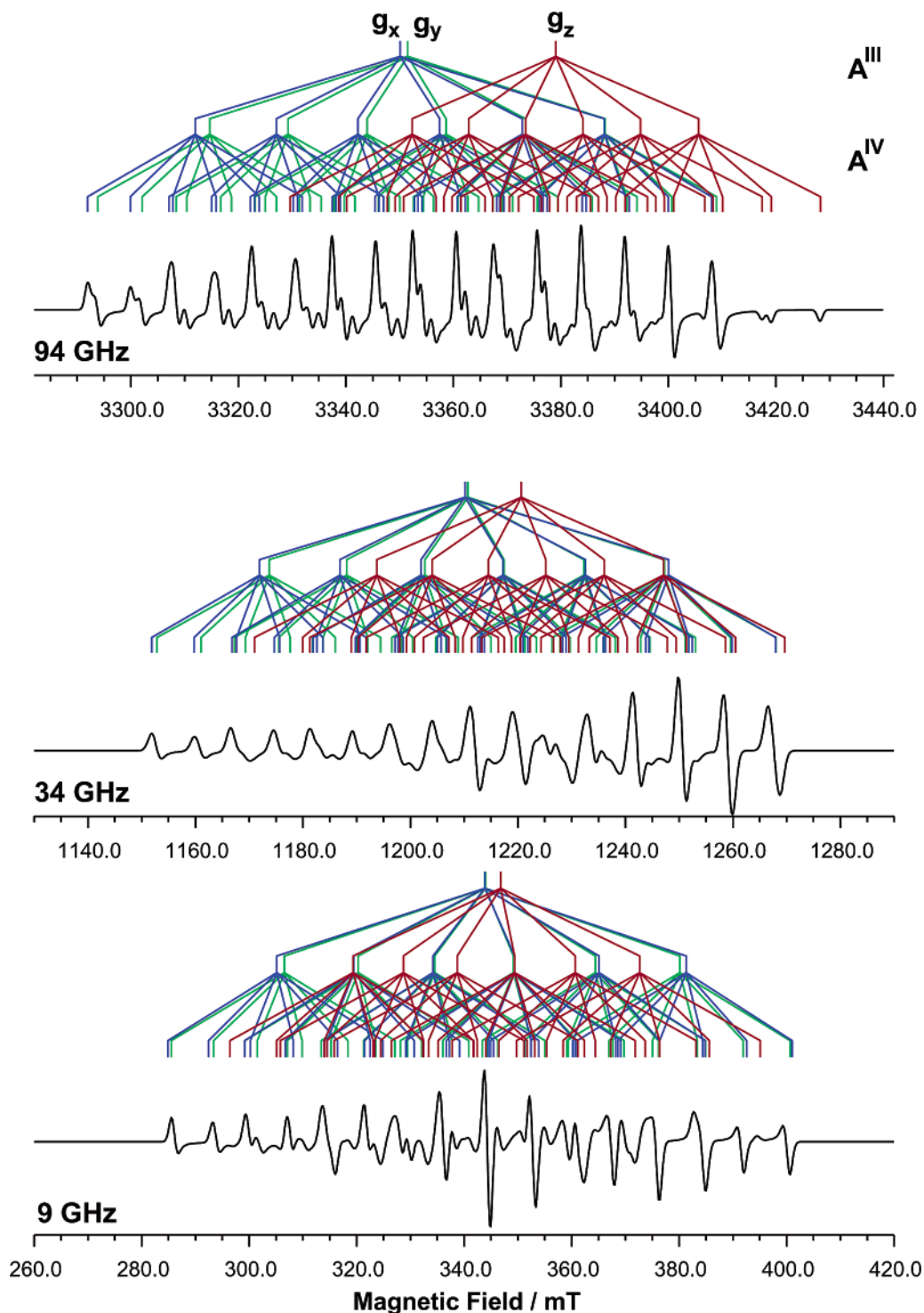


**Figure 7.** Simulated dimanganese catalase EPR spectra at 94, 34, and 9 GHz and corresponding stick diagrams. For details, see text. Magnetic field is applied along the three principal axes to construct the stick diagrams. Red: field applied along  $z$ ; blue: field applied along  $x$ ; green: field applied along  $y$ .

which lead to intermolecular spin–spin interactions. This aggregation can be avoided at lower concentrations or when  $\text{CH}_2\text{Cl}_2$  is added.

With these mixtures spin–spin interactions are suppressed and higher concentrations (5 mmol/L) can be used resulting in better signal-to-noise ratios. For the complexes TACN, DTNE, and MDTN, DMF can be used as a solvent. Here, using the pure solvent, line widths are only slightly broader than in  $\text{CH}_2\text{Cl}_2$ /DMF mixtures. As seen from Figure 6, for complex BIPY, the narrowest lines exhibit a width of about 1.3 mT at 9 GHz. With the exception of catalase, this value is obtained in

all model complexes. For our later estimation, we assume that these values represent the line widths not broadened by the above-discussed mechanisms.

**G-Strain.** The increase of line widths at higher EPR frequencies, as observed for the synthetic complexes, is due to occurrence of slightly different  $G$ -values in the samples, a phenomenon called  $G$ -strain. In particular, the  $G$ -values have been found to depend on the distance between  $\text{Mn}^{\text{III}}$  and the axially ligated nitrogens and an estimate for the broadening due to variations of that distance has been given.<sup>24</sup> To investigate this strain, it is necessary to eliminate all other sources of line



broadening, like power saturation effects or intermolecular spin–spin coupling.

To evaluate the magnitude of the  $G$ -strain in the model complexes, a natural line width that represents pure homogeneous broadening was calculated by simulating a single line using all hydrogen and nitrogen hfc's. These data were available from ENDOR experiments performed earlier on these complexes.<sup>19</sup> In these simulations, line shapes were assumed to be Lorentzian with a width of 250 kHz. For TACN, DTNE, and MDTN, the unstrained EPR line width obtained in this way was about 1.2 mT, and for BIPY and PHEN about 0.9 mT. From our experiments we obtained line widths of 1.4 mT (9 GHz), 1.7 mT (34 GHz), and 2.3 mT (94 GHz), e.g., for DTNE. This indicates, to first order, a linear dependence of the compound line width on the microwave frequency used in the experiment. From this, the increase of the line widths observed from 9 to 94 GHz would correspond to a  $\Delta G = 6 \times 10^{-4}$ .

For the catalase the strain is smaller. Line widths increase only slightly from 1.0 mT at 9 GHz to 1.1 mT at 94 GHz. In this system, the protein surrounding is well defined, in contrast to the heterogeneity caused by the microcrystalline environment found in frozen solvents. The mean deviation from the principal  $G$ -values is therefore smaller.

**Comparison with Previous Data.** Comparison with our previously published data<sup>19</sup> shows that the  $G$ -tensors have not been determined accurately enough at frequencies below 34 GHz. The hyperfine coupling tensors differ from our previous data mainly for the  $\text{Mn}^{\text{III}}$  ion. In the case of BIPY, the single largest deviation is 0.4 mT in the  $A_z^{\text{III}}$  component. For other complexes, the differences are smaller. For  $\text{Mn}^{\text{IV}}$ , deviations are within 0.1 mT, except for the  $A_x^{\text{IV}}$  component in TACN, where it is 0.2 mT. These changes are still small compared to the line widths, which limits the accurate determination of these parameters. This shows that the hyperfine data can be determined reasonably well at low frequencies.

For the dimanganese catalase, so far only low-frequency spectra have been published and simulation data are rare.<sup>17,18</sup> A simulation using the data given by Zheng et al.<sup>17</sup> was in very good agreement with our 9 GHz spectrum. At 34 and 94 GHz, however, the agreement was worse, indicating that the hfc's were determined quite well, but the  $G$ -tensor components were not. The data from our simulations differ from those of Zheng et al. only with respect to the  $G$ -tensor and the  $z$ -component of the  $\text{Mn}^{\text{III}}$  hf-tensor. This is a result of the improved accuracy we obtained for the  $G$ -tensor at 94 GHz. Since the hf-tensor  $z$  components are partially resolved in the 94 GHz spectrum, the accuracy for these components is improved compared to 9 GHz, where the  $z$  components are usually hidden and are the least accurate. Our  $G$ -tensor is slightly rhombic and has a larger anisotropy than that in ref 17. Even though the changes in the anisotropy ( $\Delta G_{xz} = G_x - G_z = 0.0172$  here vs 0.014 in ref 17) and rhombicity ( $\Delta G_{xy} = G_x - G_y = 0.0008$  here vs 0.000 in ref 17) seem small, they lead to differences in the splitting of the resonance line positions of the corresponding canonical orientations of 5.3 and 1.3 mT, respectively, at 94 GHz and are thus readily observable. The  $\text{Mn}^{\text{III}}$  hf-tensor is also more anisotropic (see Table 1).

**Visualization of Spectral Features: Stick Diagram.** Once the parameter set is obtained, an extended computer simulation can be carried out to analyze the spectra on a fundamental basis and to deconvolute the lines in the spectra. One suitable approach is the calculation of stick diagrams, in which every resonance line is attributed to a defined spin transition. By choosing field vectors along  $x$ -,  $y$ -, or  $z$ -directions, the corre-

sponding principal tensor values can be selected. At the starting point, only the  $G$ -tensor is taken into account in the simulation. Then, the hyperfine tensors are added stepwise, starting with  $\mathbf{A}^{\text{III}}$ . In this way, each of the  $G$ -components is split into a hexet. By addition of  $\mathbf{A}^{\text{IV}}$ , each of these lines further splits into a hexet. For dimanganese catalase, this is shown in Figure 7 at three frequencies (9, 34, and 94 GHz) as an example.

It is clearly seen that at 9 GHz the outer lines belong to a single field orientation (here  $x$ ), and therefore to a single  $G$ -component (Figure 7, bottom). Because of the near axiality of this system, the  $G_y$ -components are very close to the  $G_x$ -components. The  $A_z$  value of the hf tensor is small compared to the  $A_{x,y}$  value and the  $G$ -anisotropy is smaller than the hyperfine anisotropy, therefore the  $A_z$ -branch (red in Figure 7) is completely superimposed by the  $A_{x,y}$  branches (blue and green in Figure 7). At 94 GHz, however, the  $G$ -anisotropy dominates the hf anisotropy (Figure 7, top). On the high-field side of the spectrum, isolated  $z$ -components can be observed. The  $x/y$ -components are found on the low-field side, but due to the small rhombicity of the system, they are not completely separated. An assignment of nuclear spin-states to the lines can be achieved by comparison of stick diagrams and experimental spectra. This analysis is also important for future ENDOR experiments using orientation selection.

The total spectral width of the spectra is determined by two factors: (i) unresolved hyperfine couplings (inhomogeneous broadening), and (ii) the  $G$ -anisotropy and  $^{55}\text{Mn}$  hyperfine coupling (isotropic and anisotropic part). The latter one is frequency independent to first order. Thus it is expected that a certain frequency has to be reached in order to measure an increase in total spectral width. Below that frequency, the spectral width is determined by the hyperfine splitting. The frequency at which the  $G$ -anisotropy exceeds the hf-anisotropy can be calculated according to

$$\frac{|G_i - G_j|}{G_i G_j} \frac{h\nu}{\beta} = I(A_i^{\text{III}} - A_j^{\text{III}} + A_i^{\text{IV}} - A_j^{\text{IV}}) \quad (3)$$

where the indices  $i$  and  $j$  denote the different tensor components. Such a calculation has been carried out for all our complexes. For most complexes, 34 GHz is just sufficient to reach this limit. MDTN and DTNE, which exhibit the largest  $\text{Mn}^{\text{III}}$  hf-anisotropy ( $A_y - A_z = 6$  mT and 6.6 mT, respectively), show, however, no increase at 34 GHz.

The rhombicity of the  $G$ -tensor  $\Delta G_{xy} = G_x - G_y$ , ranges from  $5 \times 10^{-4}$  (MnCat) to  $65 \times 10^{-4}$  (MDTN). At 9 GHz this is smaller than 1.2 mT and cannot be resolved. At 94 GHz, however, the splitting increases by a factor of 10. This amounts to 6–11 mT for the complexes with relatively large rhombicity (DTNE, PHEN, BIPY, and MDTN). For MnCat and TACN the respective splittings (1 and 3 mT) are still comparable to the line widths and a separation of  $x$  and  $y$  components is difficult to observe even at 94 GHz.

**Intrinsic Properties of the Mn Ions.** Now that accurate EPR data of these coupled systems are available, it would be desirable to elucidate the magnetic resonance properties of the isolated  $\text{Mn}^{\text{III}}$  and  $\text{Mn}^{\text{IV}}$  ions in the complexes according to eq 2. This procedure requires either knowledge of the intrinsic hyperfine tensors  $\mathbf{a}^{\text{III}}$  and  $\mathbf{a}^{\text{IV}}$ , to calculate the ZFS parameters  $\mathbf{d}^{\text{III}}$  and  $\mathbf{d}^{\text{IV}}$ , or vice versa. The same is true for the intrinsic  $g$ -tensors  $\mathbf{g}^{\text{III}}$  and  $\mathbf{g}^{\text{IV}}$ . There are some data on monomeric  $\text{Mn}^{\text{III}}$  and  $\text{Mn}^{\text{IV}}$  complexes in the literature.<sup>29,33–37</sup> On the basis of these data it is possible to estimate the properties of the coupled systems, to demonstrate the transfer of hyperfine anisotropy from  $\text{Mn}^{\text{III}}$  to

Mn<sup>IV</sup>,<sup>17</sup> and to correlate the rhombicity of the tensors with a distortion in the Mn–O–O–Mn plane.<sup>19</sup> However, it is not possible to account for the small variation in the *G*- and hyperfine tensors in the series TACN, DTNE, and MDTN. To do this, a theory is needed that can correlate structural data with magnetic resonance data, such as density functional theory (DFT). To our knowledge, satisfactory results for the complex systems have not yet been obtained.

On the basis of the experimental data, it can be attempted to find a correlation between the models and the catalase (s. Table 1). The *G*-tensor of dimanganese catalase has the largest isotropic value within our studied complexes. Furthermore, it shows the smallest rhombicity ( $\Delta G_{xy} = 5 \times 10^{-4}$ ), so that the *G*-tensor has nearly axial symmetry. Both the isotropic value and the anisotropy agrees best with the model complex TACN ( $\Delta G_{xy} = 20 \times 10^{-4}$ ). Given the structural similarity between catalase and TACN, this is not unexpected and shows that structural features—in particular, the type of bridging ligands—and the magnetic resonance parameters are closely related.

The isotropic part of the catalase Mn<sup>III</sup> hfc tensor is  $-13.5$  mT, which is closer to that in the carboxylate bridged models ( $-13.8$  to  $-14.4$  mT) than in BIPY and PHEN ( $\approx -16.0$  mT). Recent DFT calculations on bridged manganese dimers show that the main exchange pathways involve the  $d_{yz}/d_{yz}$  and  $d_{xz}/d_{xz}$  metal orbitals. In the mixed valent Mn<sup>III</sup>Mn<sup>IV</sup> case, the unpaired electron in the  $d_{z^2}$ -orbital of Mn<sup>III</sup> is delocalized via a crossed exchange pathway into a nonbonding Mn<sup>IV</sup>  $d_{x^2-y^2}$ -orbital<sup>38</sup> in the  $\mu$ -O bridged complexes. In the  $\mu$ -OAc bridged complexes, superexchange via this additional bridge was found to be small.<sup>39</sup> However, the tilt of the Mn<sub>2</sub>O<sub>2</sub> core introduced by this bridge enhances the aforementioned crossed exchange pathway. Therefore, the unpaired electron is even more delocalized in the  $(\mu\text{-O})_2(\mu\text{-OAc})$  bridged case. This would decrease the spin density at Mn<sup>III</sup>, thereby decreasing  $A_{iso}^{III}$ . This could account for our experimentally determined differences in the magnitude of the isotropic Mn<sup>III</sup> hfc. Ideally, an increase of the isotropic Mn<sup>IV</sup> hfc would prove that the spin density is transferred from Mn<sup>III</sup> to Mn<sup>IV</sup>. This, however, is only observed in the case of catalase. For the complexes TACN, DTNE, and MDTN the isotropic Mn<sup>IV</sup> hfc is even slightly smaller than in BIPY and PHEN. From our EPR experiments, which determine the manganese hyperfine coupling only, it cannot be concluded that the missing spin density on Mn<sup>III</sup> is transferred to the nitrogen or oxygen ligands.

## Summary and Conclusion

In this work we have shown that high-frequency EPR experiments can be performed on dinuclear manganese complexes in frozen solvents and, for the first time, also in a protein surrounding. Here, as a first step, dimanganese catalase was analyzed, for which a high-resolution X-ray structure exists. An extension to more complex systems (e.g., oxygen-evolving complex (OEC) in photosystem II) is envisaged. An important experimental aspect is the elimination of Mn<sup>II</sup> impurities which give rise to very intense lines superimposed to the spectrum of the Mn<sup>III</sup>Mn<sup>IV</sup> complex. Several ways are demonstrated to suppress such lines, i.e., (i) separation via different  $T_1$  relaxation times, (ii) different  $T_2$  relaxation times, and (iii) different transition moments, in particular using pulsed 94 GHz EPR techniques. Another problem at high frequencies is the occurrence of *G*-strain caused by a variation of the microenvironment of the polycrystalline frozen solvents used for many systems. This can be improved by employing solvents or solvent mixtures that form glasses upon freezing. In the protein, the surrounding

of the bound dimetal center is much better defined and strain effects are almost absent as demonstrated for the dimanganese catalase.

At high frequencies (94 GHz and above) the *G*-tensor components of all complexes can be determined with much higher precision than previously possible using lower microwave frequencies ( $\leq 35$  GHz). This enables an improved simulation of the spectra also at lower frequencies and yields a high precision data set for *G*- and <sup>55</sup>Mn hyperfine tensors. Such data are needed for a comparison with recent DFT calculations. Furthermore, a more precise comparison between dimanganese catalase and model complexes becomes possible. Such a comparison clearly shows close similarity between the dimanganese catalase and the TACN complex. These two complexes are also structurally very similar, i.e., they have the same bridging ligands, similar Mn–Mn distance and *J* coupling. Although all complexes measured here are quite similar, any variation of the bridging situation leads to differences in *G*- and <sup>55</sup>Mn hyperfine values, that are detectable in a sensitive way by our multifrequency EPR approach.

Comparison of the experimental data for dimanganese catalase with the model complexes shows that the isotropic *G*-value  $G_{iso}$  and the anisotropy of the *G*-tensor is closest to TACN (Table 1). Furthermore, the isotropic part of the Mn<sup>III</sup> hfc tensor  $A^{III}$  is very similar, whereas for  $A^{IV}$  the deviation is somewhat larger. In any case, TACN clearly is the closest model to dimanganese catalase. Comparison of the structures (Figure 1) shows an approximately identical bridging situation in these two systems ( $(\mu\text{-O})_2(\mu\text{-carboxylato})$ ) which agrees with the similar magnetic resonance parameters. The complexes DTNE and MDTN feature an additional geometric strain and BIPY and PHEN lack the carboxylato bridging ligand. The other ligands seem to play a less important role although they will be responsible for the remaining differences. Anyway, it is interesting to see that the spectral features and the spin Hamiltonian parameters of such a highly complex system as dimanganese catalase can be modeled quite successfully by using dimanganese complexes with appropriate bridging ligands.

Ultimately, the aim is to be able to correlate the molecular structure with the EPR parameters via computational methods, such as DFT calculations. First steps toward an understanding of the exchange coupling and spin distribution in these systems have been done, (see, e.g.,<sup>10,26,38,40,41</sup>), but future work along these lines is necessary for the interpretation of EPR data for these systems.

The extension of this experimental approach and the simulation analysis strategy to other manganese systems of higher nuclearity should, in principle, be no problem, provided that sufficient signal intensity, homogeneous systems and low Mn<sup>II</sup> impurities are obtained. Clearly, the OEC is of particular interest in this context for which a satisfying simulation of the low-frequency EPR spectra of the various paramagnetic oxidation states (S-states) has not yet been obtained.<sup>42–45</sup>

**Acknowledgment.** W. Hofbauer is gratefully acknowledged for his help with the 94 GHz measurements. This work was supported by the Deutsche Forschungsgemeinschaft Grants Lu 315/14-1 and Lu 315/16-1.

## References and Notes

- (1) Kono, Y.; Fridovich, I. *J. Biol. Chem.* **1983**, *258*, 6015.
- (2) Beyer, W. F.; Fridovich, I. *Biochemistry* **1985**, *24*, 6460.
- (3) Barynin, V. V.; Grebenko, A. I. *Dokl. Acad. Nauk. SSSR* **1986**, *286*, 461.
- (4) Allgood, J. S.; Perry, J. J. *J. Bacteriol.* **1986**, *168*, 563.



- (5) Barynin, V. V.; Whittaker, M. M.; Antonyuk, S. V. *Structure* **2001**, 9, 725.
- (6) Antonyuk, S. V.; Melik-Adamyany, V. R.; Popov, A. N.; Lamzin, V. S.; Hempstead, P. D.; Harrison, P. M.; Artymyuk, P. J.; Barynin, V. V. *Crystallogr. Rep.* **2000**, 45, 111.
- (7) Khangulov, S. V.; Barynin, V. V.; Antonyuk-Barynina, S. V. *Biochim. Biophys. Acta* **1990**, 1020, 25.
- (8) Penner-Hahn, J. E. In *Manganese Redox Enzymes*; Pecoraro, V. L., Ed.; VCH Publishers: Weinheim, 1992; p 29.
- (9) Waldo, G. S.; Yu, S.; Penner-Hahn, J. E. *Biochemistry* **1991**, 30, 10486.
- (10) Brunold, T. C.; Gamelin, D. R.; Stemmler, T. L.; Mandal, S. K.; Armstrong, W. H.; Penner-Hahn, J. E.; Solomon, E. L. *J. Am. Chem. Soc.* **1998**, 120, 8724.
- (11) Khangulov, S.; Sivaraja, M.; Barynin, V. V.; Dismukes, G. C. *Biochemistry* **1993**, 32, 4912.
- (12) Siegbahn, P. E. M. *Theor. Chem. Acc.* **2001**, 105, 197.
- (13) Siegbahn, P. E. M. *J. Comput. Chem.* **2001**, 22, 1634.
- (14) Barynin, V. V.; Vagin, A. A.; Melik-Adamyany, V. R.; Grebenko, A. I.; Khangulov, S. V.; Popov, A. N.; Andrianova, M. E.; Vainstein, A. *Dokl. Acad. Nauk. SSSR* **1986**, 288, 877.
- (15) Khangulov, S. V.; Barynin, V. V.; Voevodskaya, N. V.; Grebenko, A. I. *Biochim. Biophys. Acta* **1990**, 1020, 305.
- (16) Fronko, R. M.; Penner-Hahn, J. E.; Bender, C. J. *J. Am. Chem. Soc.* **1988**, 110, 7554.
- (17) Zheng, M.; Khangulov, S. V.; Dismukes, G. C.; Barynin, V. V. *Inorg. Chem.* **1994**, 33, 382.
- (18) Haddy, A.; Waldo, G. S.; Sands, R. H.; Penner-Hahn, J. E. *Inorg. Chem.* **1994**, 33, 2677.
- (19) Schäfer, K.-O.; Bittl, R.; Zweggart, W.; Lendzian, F.; Haselhorst, G.; Weyhermüller, T.; Wieghardt, K.; Lubitz, W. *J. Am. Chem. Soc.* **1998**, 120, 4–13120.
- (20) Whittaker, M. M.; Barynin, V. V.; Antonyuk, S. V.; Whittaker, J. W. *Biochemistry* **1999**, 38, 9126.
- (21) Peloquin, J. M.; Campbell, K. A.; Randall, D. W.; Evanchik, M. A.; Pecoraro, V. L.; Armstrong, W. H.; Britt, R. D. *J. Am. Chem. Soc.* **2000**, 122, 10926.
- (22) Boelrijk, A. E. M.; Dismukes, G. C. *Inorg. Chem.* **2000**, 39, 3009.
- (23) Boelrijk, A. E. M.; Khangulov, S. V.; Dismukes, G. C. *Inorg. Chem.* **2000**, 39, 3020.
- (24) Polcar, C.; Knüpling, M.; Frapart, Y.-M.; Un, S. *J. Phys. Chem. B* **1998**, 102, 10391.
- (25) Hofbauer, W.; Bittl, R. *J. Magn. Res.* **2000**, 147, 226.
- (26) Delfs, C. D.; Stranger, R. *Inorg. Chem.* **2001**, 40, 3061.
- (27) Blondin, G.; Girerd, J.-J. *Chem. Rev.* **1990**, 90, 1359.
- (28) Bencini, A.; Gatteschi, D. *EPR of Exchange Coupled Systems*; Springer-Verlag: Berlin, 1990.
- (29) Krzystek, J.; Telser, J.; Pardi, L. A.; Goldberg, D. P.; Hoffman, B. M.; Brunel, L. C. *Inorg. Chem.* **1999**, 38, 6121.
- (30) Gamelin, D. R.; Kirk, M. L.; Stemmler, T. L.; Pal, S.; Armstrong, W. H.; Penner-Hahn, J. E.; Solomon, E. I. *J. Am. Chem. Soc.* **1994**, 116, 2392.
- (31) Schweiger, A.; Jeschke, G. *Principles of Pulse Electron Paramagnetic Resonance*; Oxford University Press: Oxford, 2001.
- (32) Cooper, S. R.; Dismukes, G. C.; Klein, M. P.; Calvin, M. *J. Am. Chem. Soc.* **1978**, 100, 7248.
- (33) Gerritsen, H. J.; Sabisky, E. S. *Phys. Rev.* **1963**, 132, 1507.
- (34) Andresen, H. G. *J. Chem. Phys.* **1961**, 35, 1090.
- (35) Barra, A. L.; Gatteschi, D.; Sessoli, R.; Abbati, G. L.; Cornia, A.; Fabretti, A. C.; Uytterhoeven, M. G. *Angew. Chem.* **1997**, 109, 2423.
- (36) Limburg, J.; Vrettos, J. S.; Crabtree, R. H.; Brudvig, G. W.; de Paula, J. C.; Hassan, A.; Duboc-Toia, A. L. B. C.; Collomb, M. N. *Inorg. Chem.* **2001**, 40, 1698.
- (37) From, W. H.; Dorain, P. B.; Kikuchi, C. *Phys. Rev. A* **1964**, 135, 710.
- (38) McGrady, J. E.; Stranger, R. *J. Am. Chem. Soc.* **1997**, 119, 8512.
- (39) Delfs, C. D.; Turner, A.; Stranger, R. *Inorg. Chem.* **2001**, 40, 4093.
- (40) Zhao, X. G.; Richardson, W. H.; Chen, J.-L.; Li, J.; Noodleman, L.; Tsai, H.-L.; Hendrickson, D. N. *Inorg. Chem.* **1997**, 36, 1198.
- (41) Delfs, C. D.; Stranger, R. *Inorg. Chem.* **2000**, 39, 491.
- (42) Zheng, M.; Dismukes, G. C. *Inorg. Chem.* **1996**, 35, 3307.
- (43) Hasegawa, K.; Ono, T.-A.; Inoue, Y.; Kusunoki, M. *Chem. Phys. Lett.* **1999**, 300, 9.
- (44) Lakshmi, K. V.; Eaton, S. S.; Eaton, G. R.; Brudvig, G. W. *Biochemistry* **1999**, 38, 12758.
- (45) Åhring, K. A.; Pace, R. J. *Biophys. J.* **1995**, 68, 2081.
- (46) Bronstein, I. N.; Semendjajew, K. A.; Musiol, G.; Mühlig, H. *Taschenbuch der Mathematik*; Verlag Harry Deutsch: Thun und Frankfurt a. M., 1997.
- (47) Rieger, P. H. *J. Magn. Reson.* **1982**, 50, 485.
- (48) Jensen, A. F.; Su, Z.; Hansen, N. K.; Larson, F. K. *Inorg. Chem.* **1995**, 34, 4244.
- (49) Wieghardt, K.; Bossek, U.; Zsolnai, L.; Huttner, G.; Blondin, G.; Girerd, J.-J.; Babonneau, F. *J. Chem. Soc., Chem. Commun.* **1987**, 651.
- (50) The standard Euler angles ( $\theta, \psi$ , and  $\phi$ ), e.g., Bronstein<sup>46</sup> and the ones used in the perturbation routine<sup>47</sup> ( $\alpha, \beta$ , and  $\gamma$ ) correlate as follows:  $\alpha \equiv \phi$ ,  $\beta \equiv \theta$ , and  $\gamma \equiv \psi$ .